

Closing the gap between Earth-based and interplanetary mission observations: Vesta seen by VLT/SPHERE^{★,★★}

R. J.L. Fétick¹, L. Jorda¹, P. Vernazza¹, M. Marsset^{2,3}, A. Drouard¹, T. Fusco^{1,4}, B. Carry⁵, F. Marchis⁶, J. Hanuš⁷, M. Viikinkoski⁸, M. Birlan⁹, P. Bartczak¹⁰, J. Berthier⁹, J. Castillo-Rogez¹¹, F. Cipriani¹², F. Colas⁹, G. Dudziński¹⁰, C. Dumas¹³, M. Ferrais¹⁴, E. Jehin¹⁴, M. Kaasalainen⁸, A. Kryszyńska¹⁰, P. Lamy¹, H. Le Coroller¹, A. Marciniak¹⁰, T. Michalowski¹⁰, P. Michel⁵, L. M. Mugnier⁴, B. Neichel¹, M. Pajuelo^{9,15}, E. Podlewska-Gaca^{10,16}, T. Santana-Ros¹⁰, P. Tanga⁵, F. Vachier⁹, A. Vigan¹, O. Witasse¹², and B. Yang¹⁷

¹ Aix-Marseille Université, CNRS, CNES, Laboratoire d'Astrophysique de Marseille, Marseille, France
e-mail: romain.fetick@lam.fr

² Department of Earth, Atmospheric and Planetary Sciences, MIT, 77 Massachusetts Avenue, Cambridge, MA 02139, USA

³ Astrophysics Research Centre, Queen's University Belfast, BT7 1NN, UK

⁴ ONERA, The French Aerospace Lab BP72, 29 avenue de la Division Leclerc, 92322 Châtillon Cedex, France

⁵ Université Côte d'Azur, Observatoire de la Côte d'Azur, CNRS, Laboratoire Lagrange, France

⁶ SETI Institute, Carl Sagan Center, 189 Bernardo Avenue, Mountain View CA 94043, USA

⁷ Institute of Astronomy, Charles University, Prague, V Holešovičkách 2, 18000, Prague 8, Czech Republic

⁸ Department of Mathematics, Tampere University of Technology, PO Box 553, 33101 Tampere, Finland

⁹ IMCCE, Observatoire de Paris, 77 avenue Denfert-Rochereau, 75014 Paris Cedex, France

¹⁰ Astronomical Observatory Institute, Faculty of Physics, Adam Mickiewicz University, Słoneczna 36, 60-286 Poznań, Poland

¹¹ Jet Propulsion Laboratory, California Institute of Technology, 4800 Oak Grove Drive, Pasadena, CA 91109, USA

¹² European Space Agency, ESTEC – Scientific Support Office, Keplerlaan 1, Noordwijk 2200 AG, The Netherlands

¹³ TMT Observatory, 100 W. Walnut Street, Suite 300, Pasadena, CA 91124, USA

¹⁴ Space sciences, Technologies and Astrophysics Research Institute, Université de Liège, Allée du 6 Août 17, 4000 Liège, Belgium

¹⁵ Sección Física, Departamento de Ciencias, Pontificia Universidad Católica del Perú, Apartado, Lima 1761, Perú

¹⁶ Institute of Physics, University of Szczecin, Wielkopolska 15, 70-453 Szczecin, Poland

¹⁷ European Southern Observatory (ESO), Alonso de Cordova 3107, 1900 Casilla Vitacura, Santiago, Chile

Received 30 November 2018 / Accepted 12 January 2019

ABSTRACT

Context. Over the past decades, several interplanetary missions have studied small bodies in situ, leading to major advances in our understanding of their geological and geophysical properties. These missions, however, have had a limited number of targets. Among them, the NASA Dawn mission has characterised in detail the topography and albedo variegation across the surface of asteroid (4) Vesta down to a spatial resolution of ~ 20 m pixel⁻¹ scale.

Aims. Here our aim was to determine how much topographic and albedo information can be retrieved from the ground with VLT/SPHERE in the case of Vesta, having a former space mission (Dawn) providing us with the ground truth that can be used as a benchmark.

Methods. We observed Vesta with VLT/SPHERE/ZIMPOL as part of our ESO large programme (ID 199.C-0074) at six different epochs, and deconvolved the collected images with a parametric point spread function (PSF). We then compared our images with synthetic views of Vesta generated from the 3D shape model of the Dawn mission, on which we projected Vesta's albedo information.

Results. We show that the deconvolution of the VLT/SPHERE images with a parametric PSF allows the retrieval of the main topographic and albedo features present across the surface of Vesta down to a spatial resolution of ~ 20 – 30 km. Contour extraction shows an accuracy of ~ 1 pixel (3.6 mas). The present study provides the very first quantitative estimate of the accuracy of ground-based adaptive-optics imaging observations of asteroid surfaces.

Conclusions. In the case of Vesta, the upcoming generation of 30–40 m telescopes (ELT, TMT, GMT) should in principle be able to resolve all of the main features present across its surface, including the troughs and the north–south crater dichotomy, provided that they operate at the diffraction limit.

Key words. techniques: high angular resolution – techniques: image processing – methods: observational – minor planets, asteroids: individual: Vesta

* Reduced images of Table A.1 are only available at the CDS via anonymous ftp to cdsarc.u-strasbg.fr (130.79.128.5) or via <http://cdsarc.u-strasbg.fr/viz-bin/qcat?J/A+A/623/A6>

** Based on observations made with ESO Telescopes at the Paranal Observatory under programme ID 199.C-0074 (PI: P. Vernazza).

1. Introduction

The surface topography of Vesta, the second largest main belt asteroid after the dwarf planet Ceres, has been characterised in detail by the framing camera (FC; [Sierks et al. 2011](#)) on board the NASA Dawn mission. The Dawn FC mapped $\sim 80\%$ of Vesta's surface with image scales of $\sim 20 \text{ m pixel}^{-1}$. These images revealed the complex topography ([Russell et al. 2012](#); [Jaumann et al. 2012](#); [Marchi et al. 2012](#); [Schenk et al. 2012](#)) summarised below:

- The south polar region consists of two overlapping impact basins (Rheasilvia & Veneneia) and a central mound whose height rivals that of Olympic Mons on Mars. Part of the outer perimeter of the Rheasilvia basin is delimited by a steep scarp. We note that both the impact basin and the central peak were first detected by [Thomas et al. \(1997\)](#) using the *Hubble* Space Telescope.

- The surface is characterised by regions with elevated topography ($\sim 20 \text{ km}$), for example the Vestalia Terra whose southernmost part merges into the rim area of the Rheasilvia basin ([Jaumann et al. 2012](#)).

- Numerous troughs are present across Vesta's surface, especially in the equatorial and northern regions. Equatorial troughs have lengths that vary from 19 to 380 km and that can be as wide as 15 km, whereas the most prominent northern trough is 390 km long and 38 km wide ([Jaumann et al. 2012](#)).

- Vesta's cratering record shows a strong north–south dichotomy with Vesta's northern terrains being significantly more cratered than the southern ones ([Marchi et al. 2012](#)).

The images of the Dawn mission also allowed the production of a high-resolution map of the albedo across Vesta's surface, revealing the greatest variation of normal albedo of any asteroid yet observed; (the normal albedo varies between ~ 0.15 and ~ 0.6 ; [Reddy et al. 2012](#); [Schröder et al. 2014](#)).

Here we present a new set of ground-based images of Vesta acquired with VLT/SPHERE/ZIMPOL as part of our ESO large programme (ID 199.C-0074; [Vernazza et al. 2018](#)). These observations, through direct comparison with the Dawn in situ measurements, were performed with the aim of testing the ultimate resolution achieved for images acquired with this new-generation adaptive-optics (AO) system ([Beuzit et al. 2008](#); [Fusco et al. 2006, 2016](#)) and the robustness of our deconvolution algorithm, which uses a synthetic point spread function (PSF) as input. These observations were also used to determine which of the geologic features discovered by Dawn (see above) can already be identified from the ground, and to place a size limit above which these features can be retrieved. Finally, these observations were used to produce an albedo map that could be directly compared with that based on the images of the Dawn FC ([Schröder et al. 2014](#)). In summary, Vesta was used as the benchmark target for our large programme, allowing us to test and ultimately validate our different techniques of image analysis.

2. Observations and data reduction

We observed (4) Vesta with the VLT/SPHERE/ZIMPOL instrument ([Beuzit et al. 2008](#); [Thalmann et al. 2008](#); [Schmid et al. 2012](#)) at six different epochs between May 20, 2018, and July 10, 2018 (see Table A.1 for a complete list of the observations). The data reduction protocol is the same for all the targets in our large programme. We refer the reader to [Vernazza et al. \(2018\)](#) for a description of the procedure. A subset of the Vesta images

after pipeline reduction and before deconvolution are shown in Fig. B.1.

3. Deconvolution method

3.1. Recurrent deconvolution artefacts with the observed PSF

Our large programme was initially designed as follows. Each asteroid observation was followed by the acquisition of a stellar PSF, using a star of same apparent magnitude as the asteroid. The asteroid image (cropped to 500×500 pixels) and its associated PSF (same pixel size as the image) were then fed to the MISTRAL algorithm ([Mugnier et al. 2004](#)) for the deconvolution process. It appeared that for nearly 50% of the observations, the deconvolution resulted in strong artefacts at the asteroid edges, highlighted by the presence of a bright corona (see upper left panel of Fig. 2 for an example). We note that edge issues resulting from the deconvolution process have already been reported in the literature ([Marchis et al. 2006](#)).

The problem was slightly improved using myopic deconvolution ([Conan et al. 1998](#)) with the MISTRAL algorithm. In this mode, the gradient-descent algorithm estimates simultaneously the couple {object+PSF}. Specifically, the PSF observed during the night was used to compute an average optical transfer function (OTF), i.e. the Fourier transform of the PSF, and all the PSFs observed during the large programme were used to compute a variance of the OTF around the average. Using this approach, the artefact intensity was reduced but still visible. This seemed to indicate that the deconvolution issues came from the PSF itself. We further inferred that the deconvolution artefacts may arise from a mismatch between the observed stellar PSF and the true PSF during the asteroid observation. If the shape of the observed PSF is too far from that of the true PSF, the myopic deconvolution cannot completely correct this issue. Moreover, myopic (or blind) deconvolution estimates simultaneously the asteroid image and the PSF, leading to an optimisation process that depends on a large number of parameters. Consequently, the mathematical problem of myopic (or blind) deconvolution might be degenerated ([Blanco & Mugnier 2011](#)) and the minimisation algorithm might converge towards the incorrect solution. Reducing the number of parameters for the PSF is thus critical to avoid degeneracy and deconvolution issues.

3.2. Use of a parametric PSF for the deconvolution

To overcome the deconvolution issues we faced, we started using parametric PSFs instead of the stellar PSFs. The advantage of a parametric PSF lies in the flexibility of its parameters, which can be adjusted to better estimate the true PSF during our asteroid observation. We chose to model these synthetic PSFs using a Moffat profile ([Moffat 1969](#)) as such functions are widely used in astronomy to reproduce the sharp coherent peak and wide wings of PSFs in AO observations ([Andersen et al. 2006](#); [Sánchez et al. 2006](#)). Additionally, the Moffat function has the advantage that it depends on only two parameters. It is defined as

$$M(r) = \frac{\beta - 1}{\pi \alpha^2} \frac{1}{(1 + r^2/\alpha^2)^\beta}, \quad (1)$$

where r is the radius to the PSF centre, α is a scale factor, and β is the Moffat power law index. Setting $\beta > 1$ is necessary to have a finite energy. Under this condition, the multiplicative factor $(\beta - 1)/\pi \alpha^2$ in the expression ensures that the total PSF energy is equal to unity.

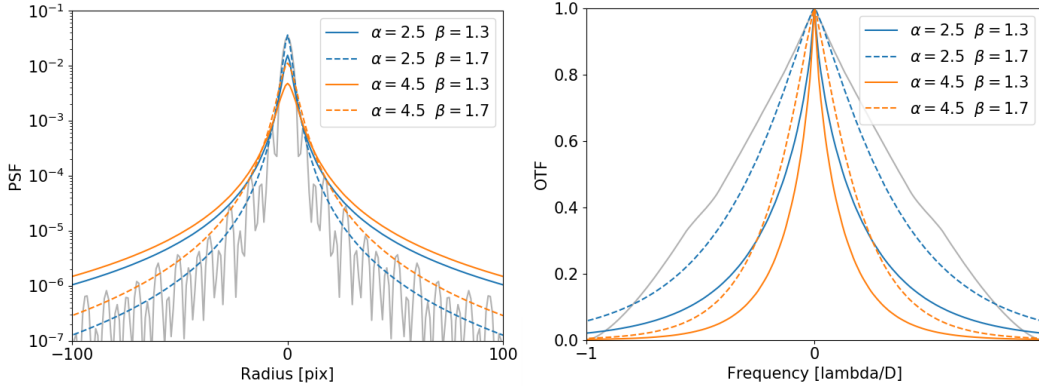


Fig. 1. Four of the 25 Moffat PSFs (*left panel*) used for deconvolution, and their associated OTF (*right panel*). Colours indicate different values of α , and line styles show different values of β . Grey curves in the left and right panels are, respectively, the PSF and OTF representing the diffraction limit of the SPHERE 8 m pupil at $\lambda = 646$ nm.

As a next step we allowed the two Moffat parameters α and β to vary within their realistic range of values: $(\alpha, \beta) \in]0, +\infty[\times]1, +\infty[$. We then determined a reasonable range of values from a visual inspection of the images: $(\alpha, \beta) \in [2.5, 4.5] \times [1.3, 1.7]$, where α is given in pixels. Figure 1 shows 4 of the 25 Moffat PSFs tested for the deconvolution of our Vesta images (for respectively the minimum and the maximum values of α and β), and highlights what we consider to be a wide range of PSF shapes for the deconvolution process.

After scanning the full range of α and β , two systematic trends were identified among the deconvolved Vesta images: a large α value in tandem with a small β value leads to the corona artefact that regularly occurred using observed PSFs (see Sect. 3.1), and a small α value in tandem with a large β value leads to under-deconvolution, meaning that the image blurring is only partially attenuated and the deconvolution is not complete (see Fig. 2).

These trends can be physically well understood when considering the fact that the full width at half maximum (FWHM) and Strehl ratio of the Moffat PSF are functions of α and β , where the FWHM can be written as

$$FWHM = 2\alpha \sqrt{2^{1/\beta} - 1}, \quad (2)$$

and the Strehl ratio as

$$\text{Strehl ratio} = \frac{M(0)}{A(0)} = \frac{\beta - 1}{\pi\alpha^2} \frac{1}{A(0)}, \quad (3)$$

with $A(0)$ being the diffraction pattern induced by the pupil (the Airy pattern for a circular non-obstructed aperture) at the centre of the PSF $r = 0$.

The diagonal behaviour observed for the deconvolution with respect to the α and β parameters (Fig. 2) makes sense when looking at the FWHM of the corresponding PSF and Strehl ratios in Fig. 2 (bottom figure). For large FWHMs (upper left corner) – or equivalently low Strehl ratios – deconvolution artefacts appear (corona artefact). This implies that the corona artefacts we encountered during the deconvolution process with observed PSFs most likely occurred either because the observed PSFs were over-estimating the FWHM of our asteroid observations or under-estimating their Strehl ratio. Inversely, for small FWHMs – or large Strehl ratios – the Vesta images appear under-deconvolved. The diagonal from bottom left to upper right shows rather stable values for both the FWHM and the Strehl ratio, in agreement with the deconvolution visual quality highlighted in

Table 1. Parameters α and β chosen for each epoch.

Epoch	α (pixel)	β
2018-05-20 06:41:53	4.0	1.5
2018-06-08 05:27:05	4.0	1.5
2018-07-10 01:59:52	4.0	1.5
2018-07-10 02:16:38	4.0	1.4
2018-06-08 07:14:40	3.0	1.5
2018-06-08 07:58:51	3.0	1.5

Fig. 2. Given the deconvolution trend as a function of the Strehl ratio (Fig. 2), we always choose α and β parameters such that the object's edges were as sharp as possible without reaching the point where the bright corona effect appears (Table 1, Fig. 2). This method has already been applied to the images acquired for (16) Psyche (Viikinkoski et al. 2018) and is now systematically applied to all targets within our large programme. In the present case, a quantitative justification (i.e. the accuracy of our deconvolved Vesta images with respect to those of the Dawn mission) for the choice of the parameters (α, β) is given in Appendix C.

In summary, the deconvolution with a Moffat PSF converges in practice toward satisfactory results. Within our large programme, we therefore started systematically using a parametric PSF with a Moffat shape to deconvolve our images. The deconvolved images of Vesta are shown in Fig. 3.

4. VLT/SPHERE compared to Dawn

In this section we determine how much topographic and albedo information can be retrieved from the ground with VLT/SPHERE in the case of Vesta, having a former space mission (Dawn) providing us with the ground truth that we can use as benchmark.

4.1. OASIS synthetic images

The NASA/Dawn in situ mission provided high-resolution images of Vesta used to generate a global shape model (Preusker et al. 2016). The images also provided the rotational parameters of the objects with a high accuracy (Konopliv et al. 2014). Knowing the ephemeris of Vesta and the position of

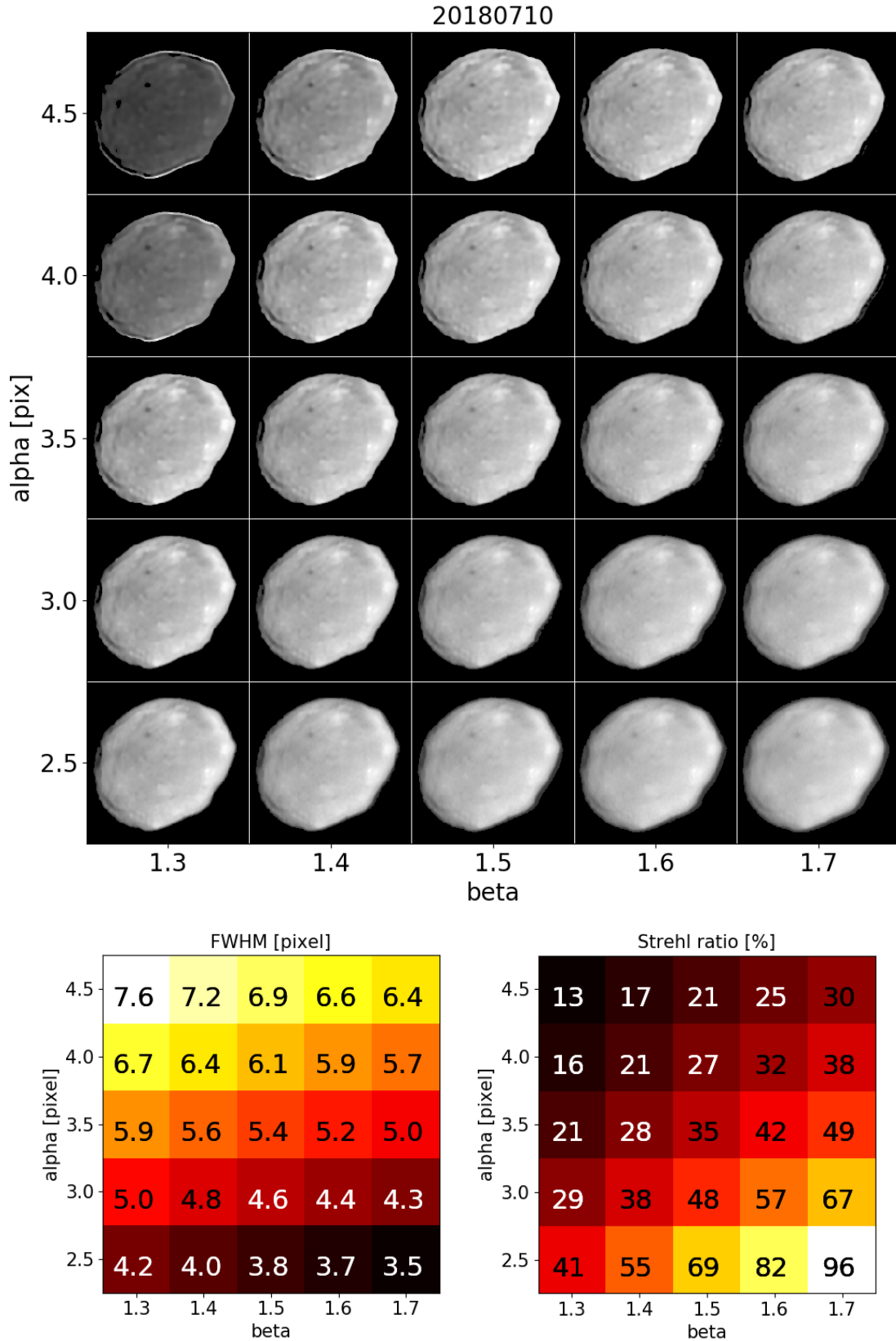


Fig. 2. *Top panels:* VLT/SPHERE/ZIMPOL observation on 2018 July 10th deconvolved using 25 different Moffat parametric PSFs. Each image of Vesta is cropped to 200×200 pixels for best enlargement, and scaled by its maximum intensity for optimum image dynamics. *Bottom panels:* corresponding FWHM and Strehl ratio for the 25 PSFs. Values indicate the FWHM and Strehl ratio, respectively, while the colour map (dark for low values, white for high values) helps to visualise the diagonal trend discussed in the text.

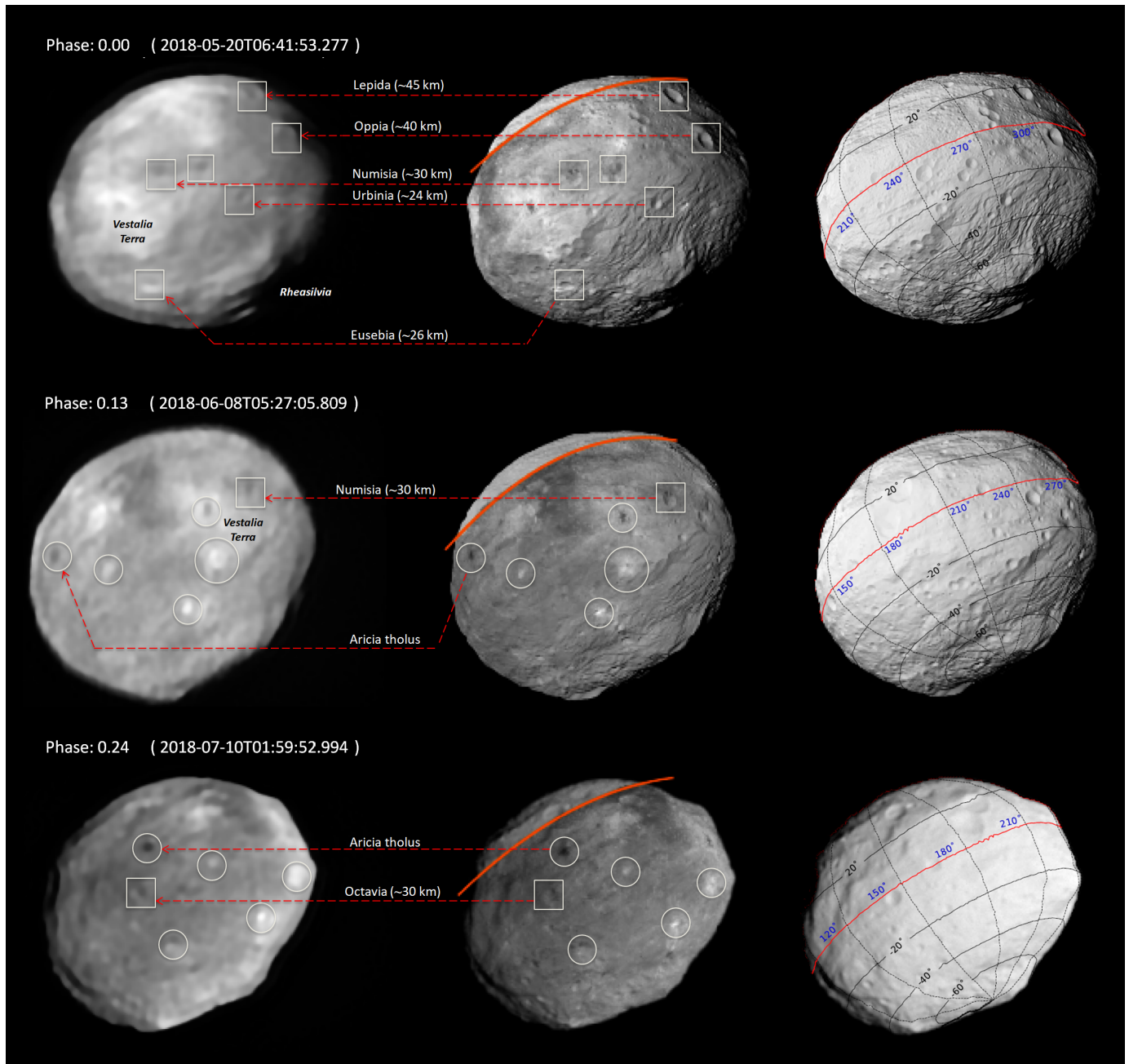


Fig. 3. Comparison of the VLT/SPHERE deconvolved images of Vesta (*left column*) with synthetic projections of the Dawn model produced with OASIS and with albedo information from Schröder et al. (2014; *middle column*), and the same projection without albedo information but with a latitude/longitude coordinate grid for reference (*right column*). All coordinates are given in the “Claudia” system (Russell et al. 2012). No albedo data is available from Dawn for latitudes above $30^{\circ}N$ (orange line). Finally, some of the main structures that can be identified in both the VLT/SPHERE images and the synthetic ones are highlighted: craters are embedded in squares and albedo features in circles. The square of the intensity is shown for the left and middle columns to highlight the surface features. Deconvolved images for the two last epochs (phase 0.43 and 0.60) show a clear-dark-clear border on the left. This deconvolution artefact seems to be the outset of the corona artefact discussed in the text.

the Earth in the J2000 Equatorial frame, it is thus possible to generate unconvolved synthetic images of Vesta at the time of the SPHERE observations. We used the OASIS tool (Jorda et al. 2010) developed and used in the frame of the Rosetta mission to create these images. The tool takes into account the pixel scale of the instrument, the viewing and illumination conditions of the object, its global shape, its rotational parameters, and the Hapke parameters describing its bi-directional reflectance properties. It rigorously accounts for cast shadows and considers

the geometric intersection between the triangular facets of the shape model and the pixels to calculate reflectance values for each pixel. We used the Hapke (1986) function built with a one-parameter Henyey-Greenstein phase function and the parameters of Li et al. (2013) to describe the reflectance of the surface. These synthetic images represent the resolution limit that could have been achieved with a turbulent-less atmosphere and perfect optics. Finally, OASIS images are multiplied by the albedo map from Schröder et al. (2014) derived from the Dawn mission

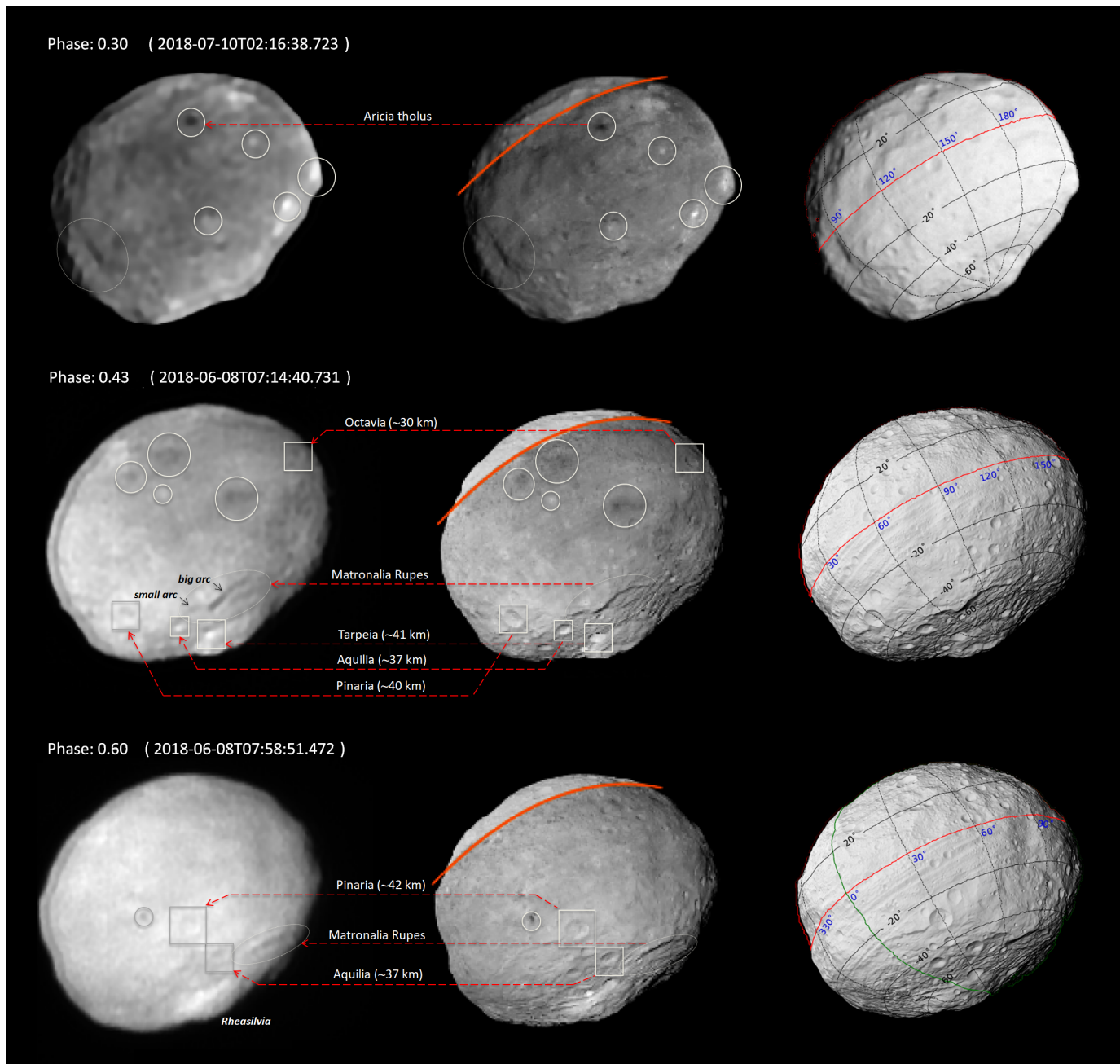


Fig. 3. continued.

and covering the southern part of Vesta up to 30°N (see Fig. 3, middle column).

4.2. Contour extraction and comparison

In order to perform a quantitative comparison between observed and synthetic OASIS images, we performed a comparison between contour plots. Contours are important for 3D shape reconstruction algorithms. The extraction of these contour plots was performed in several steps, described below. For the observed images, a low threshold T_1 was estimated by fitting the histogram of the pixels in a box of 21×21 pixels around the minimum pixel of the image. For the synthetic images, the low threshold was set to zero. A high threshold T_2 was then calculated as the maximum pixel value after

removing the 10% highest pixel values. The contour level to be used was defined as $T = T_1 + \zeta (T_2 - T_1)$, where ζ is a parameter in the interval $[0, 1]$ allowing the value of the contour level to be set with respect to the high and low thresholds. Here $\zeta = 0.3$ was chosen. The image was then converted into a triangular mesh. For this, the Cartesian coordinates of the vertices were defined by the coordinates $(X = i, Y = j)$ of the pixel (i, j) , complemented by its value $Z = P_{ij}$. Each block of 2×2 pixels allowed us to define two triangles. The resulting set of triangles represents the image as a triangular mesh. Finally, the intersection of the triangular mesh with the plane $Z = T$ defined the contour plot, represented here as a set of connected 2D points.

Let us call $\{D_i\}_{i \in [1, I]}$ and $\{M_j\}_{j \in [1, J]}$ respectively the set of points defining the deconvolved contour and the OASIS model

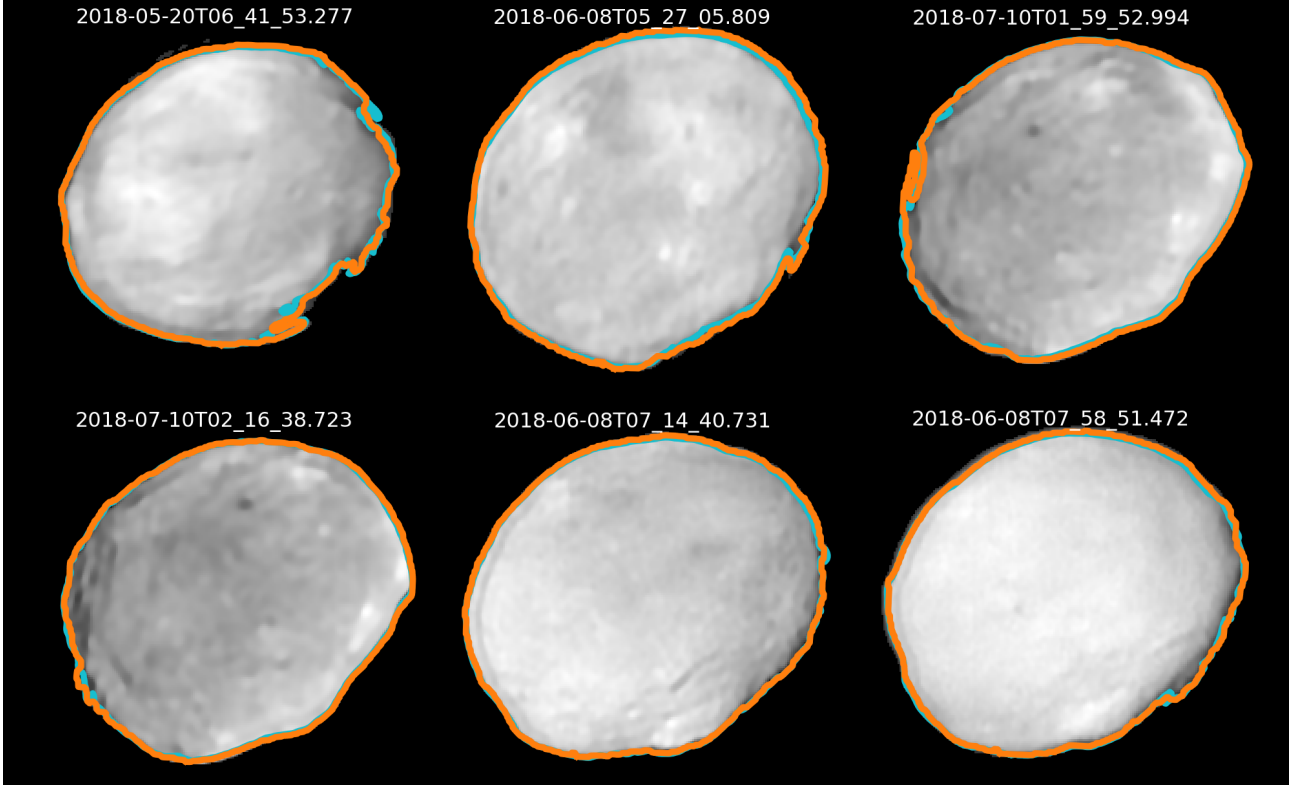


Fig. 4. Vesta contours computed for the synthetic images produced with OASIS (light blue line) and VLT/SPHERE after deconvolution (orange line). Contours are plotted over the VLT/SPHERE images for comparison.

contour. We defined the root mean square metric as

$$\chi = \sqrt{\frac{\sum_i \lambda_i \cdot d(D_i, \{M_j\}_j)^2}{\sum_i \lambda_i}}, \quad (4)$$

where the sum index i runs over all the contour points of the deconvolved image, $d(D_i, \{M_j\}_j)$ is the Euclidean distance between the point number i and its orthogonal projection onto the OASIS contour, λ_i is the pixel weighting factor. We chose λ_i to be the average distance between D_i and its neighbours D_{i-1} and D_{i+1} as

$$\lambda_i = \frac{1}{2} [d(D_i, D_{i-1}) + d(D_i, D_{i+1})], \quad (5)$$

such that an eventual cluster of close points in the contour set does not induce highly localised weighting in the χ norm. Since the points are nearly homogeneously separated, the correction has little impact on the χ norm with respect to a simple weighting $\lambda_i = 1$. Finally, forcing $\lambda_i = 0$ for some points allows us to select a specific area such as the limb or terminator for contour comparison.

Extraction of contours from the synthetic and deconvolved images shows good agreement (see Fig. 4 for contour visualisation). The match between the contours is better at the limb ($\chi_{\text{Limb}} = 0.44$ pixels) than at the terminator ($\chi_{\text{Term}} = 1.02$ pixels). Indeed the OASIS facets illumination is much more sensitive to angular errors in the orientation of the facets for nearly tangent solar rays than for normal rays. Moreover, intensity errors in the synthetic images at the terminator translate into larger errors in the contour position because the intensity gradient is smaller there compared to the large jump occurring at the limb.

The average contour error, when taking into account all contour points, is $\chi = 0.93$ pixels, showing that sub-pixel contour resolution is achievable on asteroid deconvolved images.

The area encircled by the deconvolved contour is larger than the OASIS contour with a relative area difference of +1.15%. This error might be due to residual blurring that was not fully removed by the deconvolution, and to difficulties in extracting the OASIS contour near the terminator. The resulting error on the volume would be $\sim +1.73\%$. All results concerning the contours are summarised in Table 2.

4.3. Reconnaissance of Vesta's main topographic features

It appears that most of the main topographic features present across Vesta's surface can already be recognised from the ground (Fig. 3). This includes the south pole impact basin and its prominent central mound, several $D \geq 25$ km sized craters and Matronalia Rupes including its steep scarp and its small and big arcs (Krohn et al. 2014). From these observations, we can determine a size limit of ~ 30 km for the features that can be resolved with VLT/SPHERE (i.e. features that are 8–10 pixels wide). This detection limit should be in principle sufficient to recognise the north–south crater dichotomy detected by Dawn (Marchi et al. 2012; Vincent et al. 2014), according to the fact that the northern hemisphere hosts 70% of the craters with $D \geq 30$ km (Liu et al. 2018). There are several plausible explanations as to why we were not able to resolve this dichotomy. First, we mostly imaged the southern hemisphere, due to Vesta's spin axis orientation. Second, the atmospheric blurring (not entirely removed by the AO) is another limiting factor. Third, the albedo variation across the surface is large, leading to a confusion between the shade of the craters and local albedo variation. This is clearly

Table 2. Results on the contour extraction for OASIS and deconvolved images.

Epoch (UTC)	χ (pix)	χ_{Limb} (pix)	χ_{Term} (pix)	\mathcal{A}_O (pix ²)	\mathcal{A}_D (pix ²)
2018-05-20 06:41:53	0.83	0.41	0.99	19272	19414 (+0.73%)
2018-06-08 05:27:05	1.50	0.65	1.27	22673	23382 (+3.12%)
2018-06-08 07:14:40	0.55	0.40	0.54	22762	22920 (+0.70%)
2018-06-08 07:58:51	0.60	0.42	0.71	22362	22379 (+0.52%)
2018-07-10 01:59:52	1.37	0.39	1.73	21017	21224 (+0.98%)
2018-07-10 02:16:38	0.72	0.34	0.87	21223	21402 (+0.84%)
Average \pm std	0.93 ± 0.37	0.44 ± 0.10	1.02 ± 0.39		(+1.15 \pm 0.89%)

Notes. Deconvolved images considered here are the ones from Fig. 3 obtained for the (α, β) parameters in Table 1. The χ , χ_{Limb} and χ_{Term} errors are explained in the text. Columns \mathcal{A}_O and \mathcal{A}_D are respectively the area encircled by OASIS and the deconvolution contours. Percentages inside parentheses show the relative error on the estimated deconvolved area with respect to the OASIS area.

highlighted in the synthetic images generated by OASIS with and without albedo information (see middle and right column in Fig. 3). Fourth, we do not observe the equatorial troughs of Vesta, which are 15 km wide and thus below the detection limit of our images. It follows that future generation telescopes with mirror sizes in the 30–40 m range should in principle be able to resolve the main features present across Vesta’s surface, provided that they operate at the diffraction limit.

Finally, we attempt to constrain the detection rate for the largest craters with diameter greater than 40 km. Except the large Rheasilvia basin, Vesta hosts 21 such craters (Liu et al. 2018) and 9 of them were covered by our observations. Of these nine craters, we could identify seven of them (see Fig. 3) in our images, implying a detection rate of $\sim 80\%$. The two missing craters are Marcia and Calpurnia, which are part of the snowman crater chain that is located at $\sim 13^\circ$ north latitude and $\sim 195^\circ$ eastern longitude. The non-detection of the snowman crater chain is not surprising when looking at the two synthetic OASIS images (with and without albedo information) as the crater chain can barely be recognised in the synthetic images with albedo information (see Fig. 5).

4.4. Reconnaissance of Vesta’s main albedo features

To further test the reliability of the observation and deconvolution procedure, we built an albedo map of Vesta from the deconvolved SPHERE images, and compared this map to that of Schröder et al. (2014) from in situ Dawn measurements. We used a subsample of 19 high-quality images from the six epochs of VLT/SPHERE observations.

Owing to the limited number of geometrical views probed by SPHERE, it is not always possible to differentiate shadows from true albedo variations without prior knowledge about the local surface topography. This information is very well constrained in the case of Vesta, and can be retrieved from the OASIS model. However, this is not true for most targets in our observing programme, and for almost all asteroids in general. We therefore purposely did not use any prior information on Vesta’s topography when building the map in order to evaluate our ability to retrieve albedo information from the SPHERE observations alone.

First, we corrected the illumination gradient present in the SPHERE images, which depends on the local incidence, reflection, and phase angle. This was performed by fitting a second-order polynomial surface to the disc (image intensity) of Vesta. This method provides satisfactory results for Earth-based observations of asteroids (Carry et al. 2008, 2010). Across our

observing programme, we also found that it provides better results than using a scattering law (Lommel–Seeliger, Hapke; Li et al. 2015) when little is known about the local topography of the object. Using one of the above-mentioned scattering laws with a low-resolution shape model indeed results in artificially “paved” images owing to the resolution, i.e. the size of the facets, in the model. The use of a polynomial fit, which qualitatively mimics the Lommel–Seeliger laws, to the disc of the object results in smoother photometric correction without artificial discontinuities. However, it cannot properly fit the illumination of local terrain features, such as craters and mountains.

For each SPHERE image, we then defined a region of interest (ROI) containing the set of pixels to be projected on the map. As discussed in Sect. 3, an over-deconvolution usually enhances the brightness of the image regions with strong luminosity gradient, such as the asteroid border. To avoid including pixels affected by this effect, we only considered pixels contained in the central region of the asteroid, i.e. 20 pixels away from the asteroid contour (limb and terminator).

Next, the longitude and latitude of each pixel contained in the ROI was measured using a projection of the OASIS model (Sect. 4.1). For other targets in our programme, this would be performed using a lower resolution model derived with the ADAM software (Viikinkoski et al. 2015).

Each pixel value was then projected on the map, using an equidistant cylindrical projection. The individual maps from the different epochs of observation were then combined using the overlapping regions to balance their brightness level. Specifically, the combined map was calculated as a weighted average of the individual maps, where each pixel was attributed a Gaussian weight inversely proportional to the projected surface area it covers, and inversely proportional to its projected distance from the sub-Earth point. Finally, we normalised the combined map with the global average albedo of Vesta in the Johnson *V* band (centred on 540 nm) in order to allow a direct comparison with the albedo map of Schröder et al. (2014).

The resulting map is shown and compared to that of Schröder et al. (2014) in Fig. 5. The Dawn map displays only the region of Vesta seen by SPHERE in order to facilitate the comparison. Other pixels were set to zero.

The SPHERE map exhibits a wide range of albedo values (typically $A_{V,N} = 0.34\text{--}0.45$), close to that of Dawn (mostly $A_{V,N} = 0.30\text{--}0.46$), but slightly narrower owing to its lower spatial resolution and residual blurring due to imperfect deconvolution (Fig. 6). The peak of the two distributions is slightly offset, due to the different shape of the distributions: the SPHERE distribution appears even on both sides of the peak, whereas the

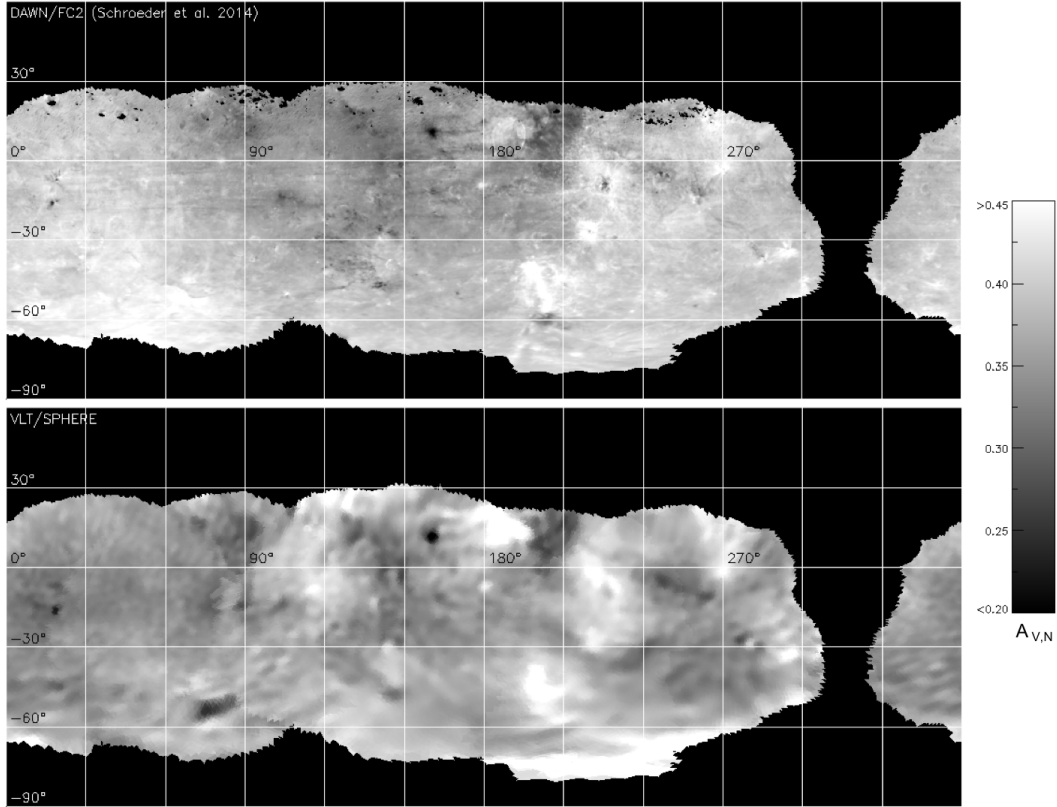


Fig. 5. Albedo map of Vesta constructed from VLT/SPHERE images (*bottom panel*) compared to the Dawn Framing Camera 2 (FC2) map derived in situ (*top panel*; Schröder et al. 2014). The two maps are in equidistant cylindrical projection. The Dawn map only shows the region of Vesta covered by SPHERE to facilitate the comparison. The north region of the Dawn map, with the latitude ϕ in the $[0^\circ, +30^\circ]$ range, contains several pixels with no available information. Those pixels are left black.

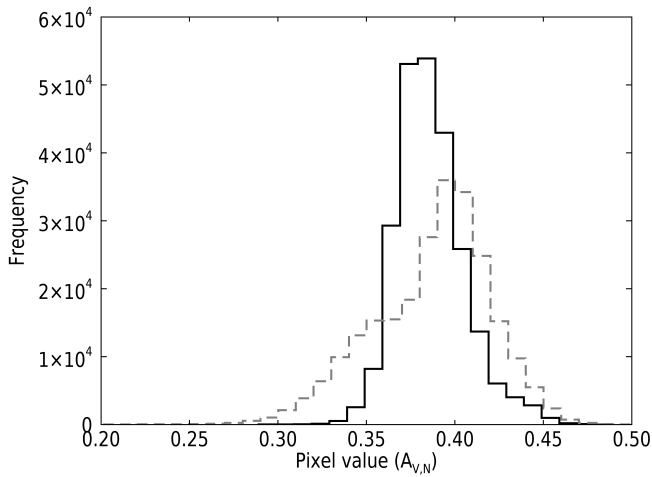


Fig. 6. Histogram of pixel values for the SPHERE (continuous black) and Dawn (dotted grey) albedo maps. The SPHERE map exhibits a slightly narrower range of albedo values with respect to Dawn, owing to its lower spatial resolution and residual blurring of the images due to imperfect deconvolution.

low-end tail of the Dawn distribution is wider than the high-end one, possibly because multiple species with different albedos are spatially resolved. Most of the main albedo features present in the Dawn map can also be identified in the SPHERE map. We find that surface features down to 20 km in size can be identified from the SPHERE map.

Only a few inconsistencies between the two maps are found. The most obvious example is the presence of a dark region located near $\lambda = 80^\circ, \phi = -50^\circ$ on the SPHERE map, whereas Dawn finds no such albedo variation at this location. This feature most likely results from the presence of shadows in the SPHERE images caused by irregular terrains rather than true albedo variations. The brightness of the southernmost region of Vesta on the map for $\lambda \in [180^\circ, 270^\circ]$ and $\phi < -60^\circ$ is enhanced with SPHERE compared to Dawn. This is due to the illumination of the Rheasilvia central peak, which could not be accurately corrected. The Dawn map contains very localised regions with very low albedo values ($A_{V,N} < 0.25$). While these regions are also seen with SPHERE, they display higher albedos ($A_{V,N} > 0.30$) due to the lower spatial resolution of the map that attenuates the high-frequency albedo variations. Additional differences between the two maps may arise from the different filters used during the observations: ZIMPOL N_R ($\lambda = 589.2\text{--}702.6$ nm) versus DAWN FC2 clear filter ($\lambda = 438\text{--}965$ nm).

5. Conclusion

In this article, we evaluated how much topographic and albedo information can be retrieved from the ground with VLT/SPHERE in the case of the asteroid (4) Vesta. This object can be used as a benchmark for ground-based observations since the Dawn space mission provided us with ground truth information. We observed (4) Vesta with VLT/SPHERE/ZIMPOL as part of our ESO large programme at six different epochs, and deconvolved the collected images with a parametric PSF.

We then compared our VLT/SPHERE images with synthetic images of Vesta produced with the OASIS software that uses the 3D shape model of the Dawn mission as input and on which we re-projected the albedo map of the Dawn mission (Schröder et al. 2014). We further produced our own albedo map of Vesta from the SPHERE images alone, and without using any prior information about the surface topography of Vesta. We compared this map to that of Schröder et al. (2014) to evaluate our ability to differentiate true albedo variegation from shadows and regions with enhanced illumination due to imperfect photometric correction of the SPHERE images.

We show that the deconvolution of the VLT/SPHERE images with a parametric PSF allows the retrieval of the main topographic and albedo features present across Vesta's surface down to a spatial resolution of ~20–30 km. Contour extraction shows a precision of ~1 pixel, with a strong difference between the estimation of the limb (precision of ~0.5 pixel) and the terminator (precision of ~1 pixel). The consequent relative error on the estimated area is $\leq 2\%$.

The present study demonstrates for the very first time the accuracy of ground-based AO imaging observations of asteroids with respect to in situ observations. Future generation telescopes (ELT, TMT, GMT) could use Vesta as a benchmark to catch all of the main features present across its surface (including the troughs and the north–south crater dichotomy), provided that these telescopes operate at the diffraction limit.

Data retrieval: as soon as papers for our large programme are accepted for publication, we will make the corresponding reduced and deconvolved AO images and 3D shape models publicly available¹.

Acknowledgements. This work was supported by the French Direction Générale de l'Armement (DGA) and Aix-Marseille Université (AMU). P.V., A.D., and B.C. were supported by CNRS/INSU/PNP. J.H. was supported by the grant 18-09470S of the Czech Science Foundation and by the Charles University Research Programme No. UNCE/SCI/023. This project has received funding from the European Union's Horizon 2020 research and innovation programme under grant agreement No. 730890. This material reflects only the authors' views and the Commission is not liable for any use that may be made of the information contained herein. The authors thank S. Schröder for providing his reconstructed albedo map based on the Dawn images and for his very fruitful comments as a referee.

References

- Andersen, D. R., Stoesz, J., Morris, S., et al. 2006, *PASP*, **118**, 1574
- Beuzit, J.-L., Feldt, M., Dohlen, K., et al. 2008, in *Ground-based and Airborne Instrumentation for Astronomy II*, *SPIE*, **7014**, 701418
- Blanco, L., & Mugnier, L. M. 2011, *Opt. Express*, **19**, 23227
- Carry, B., Dumas, C., Fulchignoni, M., et al. 2008, *A&A*, **478**, 235
- Carry, B., Dumas, C., Kaasalainen, M., et al. 2010, *Icarus*, **205**, 460
- Conan, J.-M., Mugnier, L. M., Fusco, T., Michau, V., & Rousset, G. 1998, *Appl. Opt.*, **37**, 4614
- Fusco, T., Petit, C., Rousset, G., et al. 2006, *Proc. SPIE*, **6272**, 62720K
- Fusco, T., Sauvage, J.-F., Mouillet, D., et al. 2016, in *Adaptive Optics Systems V*, *Proc. SPIE*, **9909**, 99090U
- Hapke, B. 1986, *Icarus*, **67**, 264
- Jaumann, R., Williams, D. A., Buczkowski, D. L., et al. 2012, *Science*, **336**, 687
- Jorda, L., Spjuth, S., Keller, H. U., Lamy, P., & Llebaria, A. 2010, *Proc. SPIE*, **7533**, 75331I
- Konopliv, A. S., Asmar, S. W., Park, R. S., et al. 2014, *Icarus*, **240**, 103
- Krohn, K., Jaumann, R., Otto, K., et al. 2014, *Icarus*, **244**, 120
- Li, J.-Y., Le Corre, L., Schröder, S. E., et al. 2013, *Icarus*, **226**, 1252
- Li, J. Y., Helfenstein, P., Buratti, B., Takir, D., & Clark, B. E. 2015, *Asteroid IV* (Tucson, AZ: University of Arizona Press), 129
- Liu, Z., Yue, Z., Michael, G., et al. 2018, *Icarus*, **311**, 242
- Marchi, S., McSween, H. Y., O'Brien, D. P., et al. 2012, *Science*, **336**, 690
- Marchis, F., Kaasalainen, M., Hom, E. F. Y., et al. 2006, *Icarus*, **185**, 39
- Moffat, A. 1969, *A&A*, **3**, 455
- Mugnier, L. M., Fusco, T., & Conan, J.-M. 2004, *JOSA A*, **21**, 1841
- Preusker, F., Scholten, F., Matz, K.-D., et al. 2016, *NASA Planetary Data System*, **268**, DAWN
- Reddy, V., Nathues, A., Le Corre, L., et al. 2012, *Science*, **336**, 700
- Russell, C. T., Raymond, C. A., Coradini, A., et al. 2012, *Science*, **336**, 684
- Sánchez, F. M., Davies, R., Eisenhauer, F., et al. 2006, *A&A*, **454**, 481
- Schenk, P., O'Brien, D. P., Marchi, S., et al. 2012, *Science*, **336**, 694
- Schmid, H.-M., Downing, M., Roelfsema, R., et al. 2012, in *Ground-based and Airborne Instrumentation for Astronomy IV*, *Proc. SPIE*, **8446**, 84468Y
- Schröder, S. E., Mottola, S., Keller, H. U., Raymond, C. A., & Russell, C. T. 2014, *Planet. Space Sci.*, **103**, 66
- Sierks, H., Keller, H. U., Jaumann, R., et al. 2011, *Space Sci. Rev.*, **163**, 263
- Thalmann, C., Schmid, H. M., Boccaletti, A., et al. 2008, in *Ground-based and Airborne Instrumentation for Astronomy II*, *Proc. SPIE*, **7014**, 70143F
- Thomas, P. C., Binzel, R. P., Gaffey, M. J., et al. 1997, *Science*, **277**, 1492
- Vernazza, P., Brož, M., Drouard, A., et al. 2018, *A&A*, **618**, A154
- Viikinkoski, M., Kaasalainen, M., & Durech, J. 2015, *A&A*, **576**, A8
- Viikinkoski, M., Vernazza, P., Hanuš, J., et al. 2018, *A&A*, **619**, L3
- Vincent, J.-B., Schenk, P., Nathues, A., et al. 2014, *Planet. Space Sci.*, **103**, 57

¹ <http://observations.lam.fr/astero/>

Appendix A: Observation table**Table A.1.** Vesta images.

Date	UT	Airmass	Δ (AU)	r (AU)	α ($^{\circ}$)	D_a ($''$)
2018-05-20	6:41:53	1.01	1.25	2.15	15.8	0.579
2018-05-20	6:43:24	1.01	1.25	2.15	15.8	0.579
2018-05-20	6:44:56	1.01	1.25	2.15	15.8	0.579
2018-05-20	6:46:25	1.01	1.25	2.15	15.8	0.579
2018-05-20	6:47:56	1.01	1.25	2.15	15.8	0.579
2018-06-08	5:27:05	1.01	1.16	2.15	6.8	0.624
2018-06-08	5:28:36	1.01	1.16	2.15	6.8	0.624
2018-06-08	5:30:08	1.01	1.16	2.15	6.8	0.624
2018-06-08	5:31:38	1.00	1.16	2.15	6.8	0.624
2018-06-08	5:33:07	1.00	1.16	2.15	6.8	0.624
2018-06-08	7:14:40	1.08	1.16	2.15	6.7	0.624
2018-06-08	7:16:10	1.09	1.16	2.15	6.7	0.624
2018-06-08	7:17:42	1.09	1.16	2.15	6.7	0.624
2018-06-08	7:19:12	1.09	1.16	2.15	6.7	0.624
2018-06-08	7:20:41	1.10	1.16	2.15	6.7	0.624
2018-06-08	7:58:51	1.19	1.16	2.15	6.7	0.624
2018-06-08	8:00:22	1.19	1.16	2.15	6.7	0.624
2018-06-08	8:01:51	1.20	1.16	2.15	6.7	0.624
2018-06-08	8:03:21	1.20	1.16	2.15	6.7	0.624
2018-06-08	8:04:52	1.21	1.16	2.15	6.7	0.624
2018-07-10	1:59:52	1.04	1.19	2.16	10.9	0.608
2018-07-10	2:01:24	1.03	1.19	2.16	10.9	0.608
2018-07-10	2:02:56	1.03	1.19	2.16	10.9	0.608
2018-07-10	2:04:25	1.03	1.19	2.16	10.9	0.608
2018-07-10	2:05:56	1.03	1.19	2.16	10.9	0.608
2018-07-10	2:16:38	1.02	1.19	2.16	10.9	0.608
2018-07-10	2:18:09	1.02	1.19	2.16	10.9	0.608
2018-07-10	2:19:39	1.02	1.19	2.16	10.9	0.608
2018-07-10	2:21:09	1.02	1.19	2.16	10.9	0.608
2018-07-10	2:22:39	1.02	1.19	2.16	10.9	0.608

Notes. For each observation, the table gives the epoch, the airmass, the distance to the Earth Δ and the Sun r , the phase angle α , and the angular diameter D_a . All observations were performed on the VLT/SPHERE instrument, with N_R filter, and 80 s of exposure time.

Appendix B: Additional figure

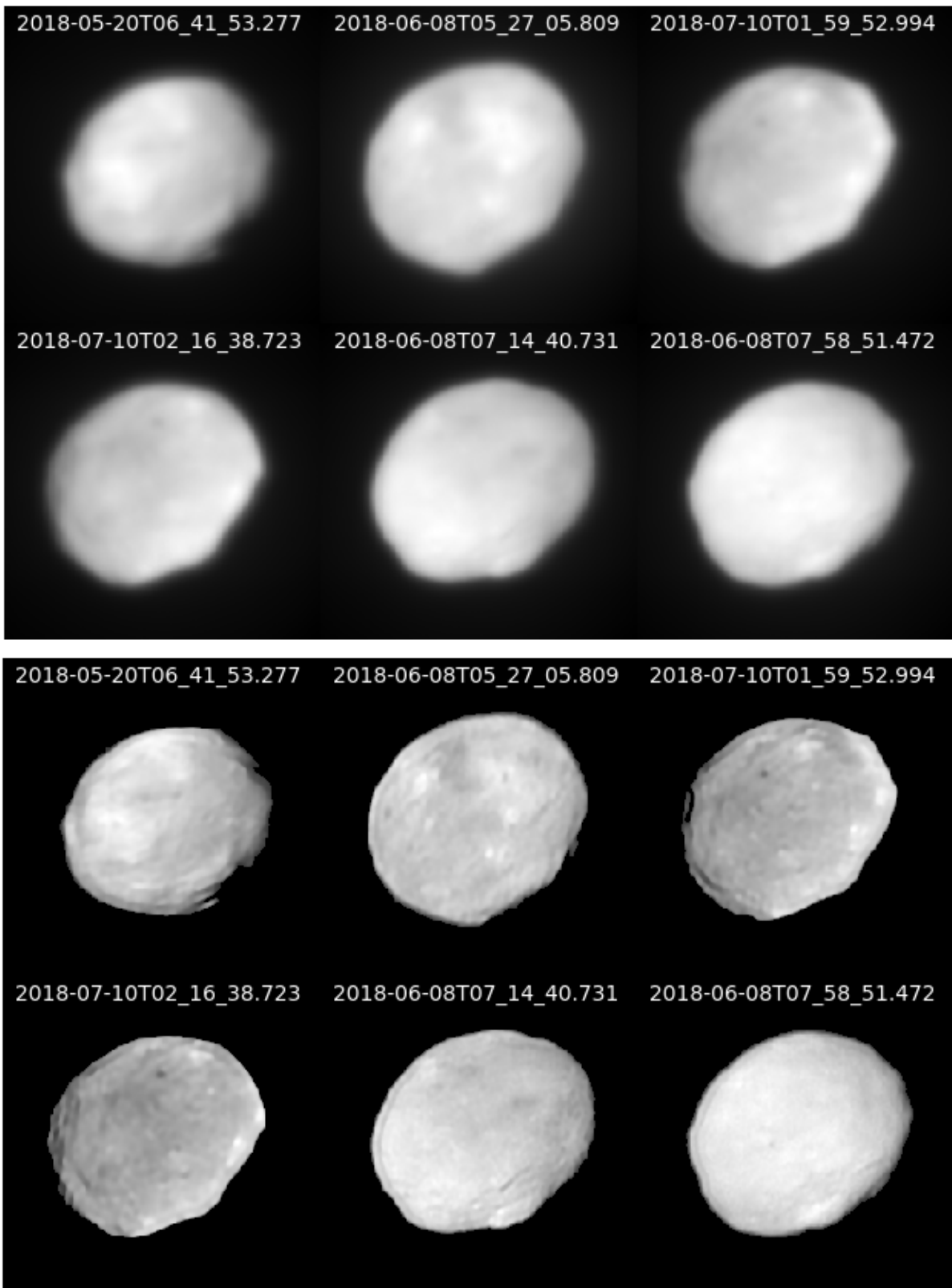


Fig. B.1. *Top panel:* reduced Vesta images after pipeline. *Bottom panel:* same images after deconvolution.

Appendix C: Optimisation of the PSF parameters

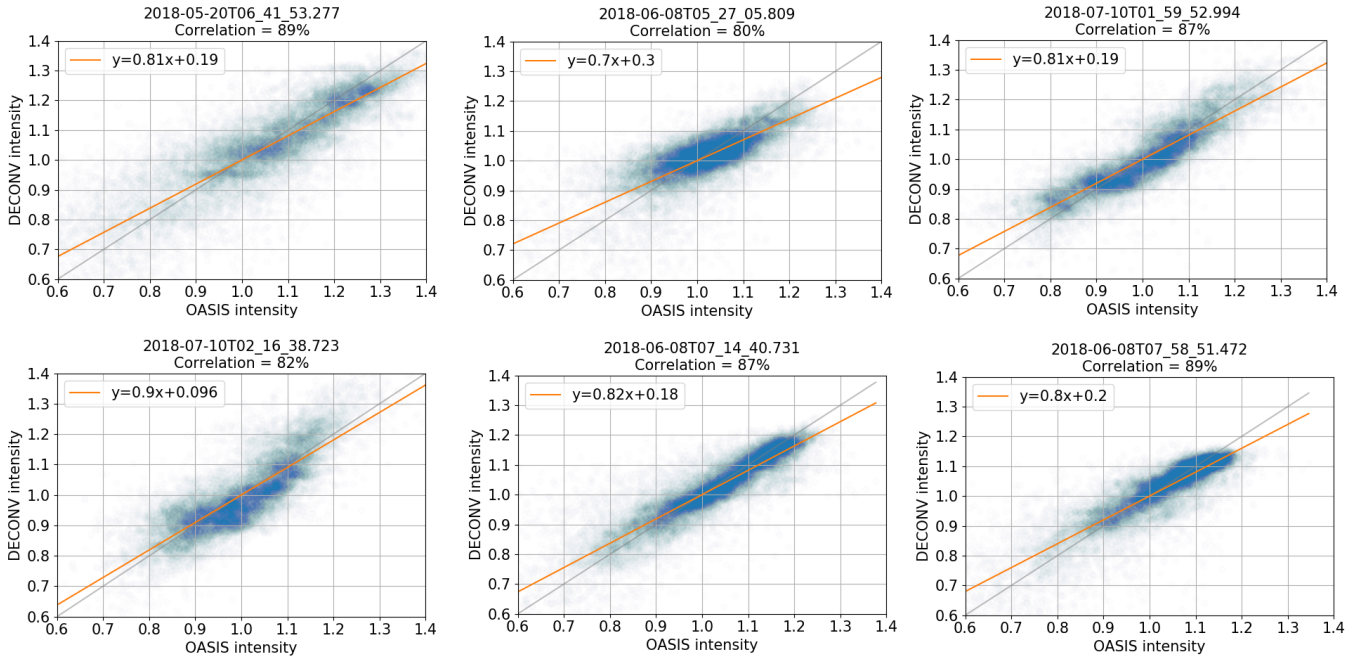


Fig. C.1. Correlation between OASIS (including albedo) and deconvolved image pixel intensities. Each intensity map has been divided by its average value for normalisation. Each of the six graphs corresponds to an epoch of observation. The linear fit of each cloud of points is also shown (orange line). The correlation percentage between OASIS and deconvolution intensities is written at the top of each graph.

Using OASIS synthetic images with albedo, we were also able to determine the optimal values of α and β for the deconvolution by calculating the root square error between the deconvolved SPHERE/ZIMPOL images and the synthetic images (OASIS+albedo model). The error writes as

$$\epsilon(\alpha, \beta) = \sqrt{\sum_p (\text{DEC}_p(\alpha, \beta) - a_p \times \text{OAS}_p)^2}, \quad (\text{C.1})$$

where the sum runs over the pixels, OAS is the OASIS model multiplied by the albedo a_p corresponding to each pixel, and DEC is our deconvolved image. When writing $\text{DEC}_p(\alpha, \beta)$ we recall that the deconvolution depends on the PSF parameters (α, β) . The minimisation of the error $\epsilon(\alpha, \beta)$ identifies the optimal values for the α and β parameters and thus the most accurate deconvolution in the sense of the norm given by Eq. (C.1). Figure C.2 shows the evolution of ϵ with respect to the PSF parameters α and β for the six epochs. The minimum is reached

in the narrow range $\alpha \simeq 3.5\text{--}4$ and $\beta \simeq 1.5\text{--}1.6$. Figure C.2 also shows that the error increases dramatically when the corona artefact appears, and that the minimum error is reached for sharp deconvolutions just before the corona effect.

Thus, the (α, β) parameters empirically estimated in Sect. 3.2 are close to the actual optimal values that minimise the ϵ criteria. Near such optimal values, only the corona effect may corrupt the deconvolution result at high α and low β . Otherwise the deconvolution zone is stable since the deconvolution quality evolves continuously with the parameters (see Figs. 2 and C.2).

Importantly, we believe that it is possible to further improve the deconvolution procedure using even more accurate PSF models, with a shape closer to that of the AO corrected PSF (paper in preparation on the AO PSF modelling). Finally, PSF parameters (whatever PSF model is used) may be estimated automatically by a myopic deconvolution algorithm, such as Mugnier et al. (2004) and Blanco & Mugnier (2011).

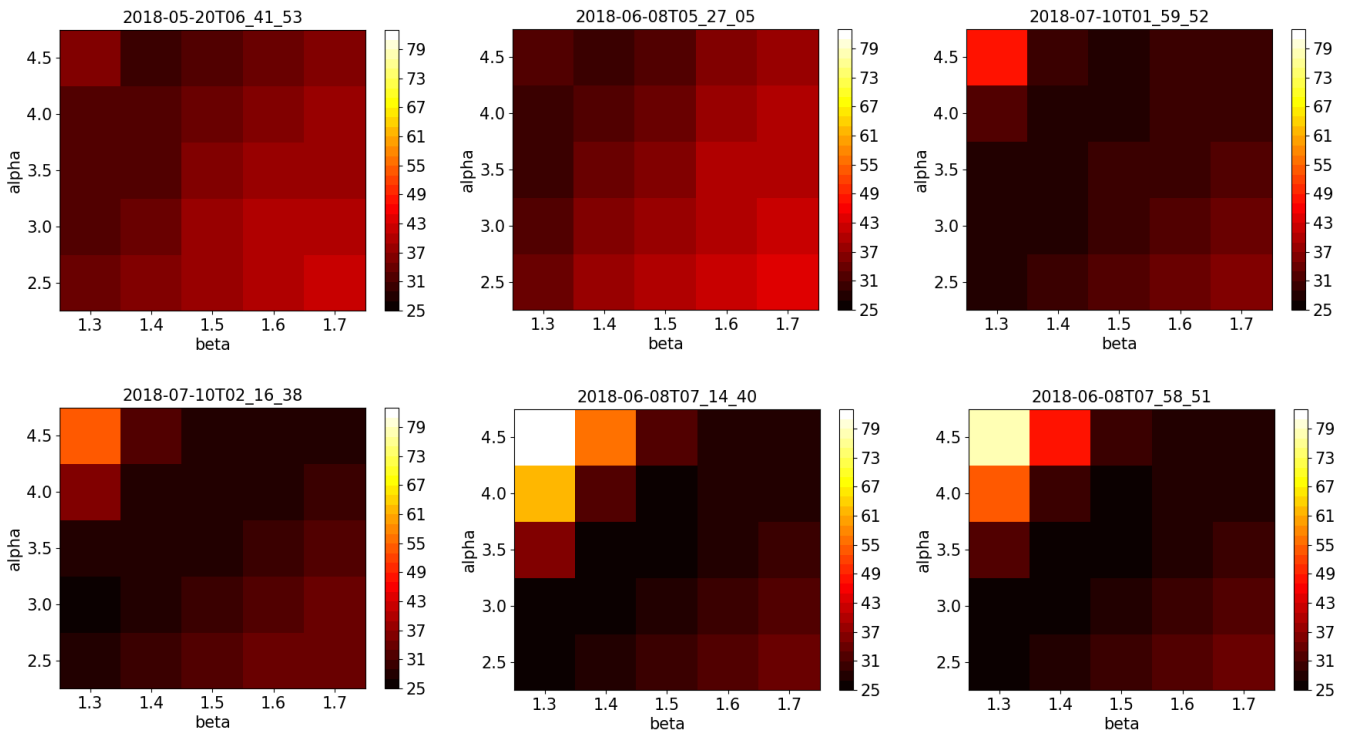


Fig. C.2. Root square error between deconvolved images and OASIS+albedo model. Each of the six subfigures corresponds to one of the observing epoch. Evolution of the error with respect to the α and β parameters is then visible. For each epoch, optimal values of α and β are the ones that minimise the error. Invalid pixels (missing albedo) were removed for error computation. However, all pixels (inside and outside the asteroid) are considered to take into account the residual blurring after eventual incomplete deconvolution. Errors have also been divided by the flux of each Vesta observation so they reach comparable values between the different epochs.